ULTRA-FAINT ULTRAVIOLET GALAXIES AT $z \sim 2$ BEHIND THE LENSING CLUSTER A1689: THE LUMINOSITY FUNCTION, DUST EXTINCTION, AND STAR FORMATION RATE DENSITY*

Anahita Alavi[1], Brian Siana[1], Johan Richard[2], Daniel P. Stark[3], Claudia Scarlata[4], Harry I. Teplitz[5],
William R. Freeman[1], Alberto Dominguez[1], Marc Rafelski[5], Brant Robertson[3], and Lisa Kewley[6]

[1] Department of Physics and Astronomy, University of California, Riverside, CA 92521, USA; anahita.alavi@email.ucr.edu
[2] Centre de Recherche Astrophysique de Lyon, Université Lyon 1, 9 Avenue Charles André, F-69561 Saint Genis Laval Cedex, France
[3] Department of Astronomy, Steward Observatory, University of Arizona, 933 North Cherry Avenue, Rm N204, Tucson, AZ 85721, USA
[4] Minnesota Institute for Astrophysics, University of Minnesota, Minneapolis, MN 55455, USA
[5] Infrared Processing and Analysis Center, Caltech, Pasadena, CA 91125, USA
[6] Research School of Astronomy and Astrophysics, The Australian National University, Cotter Road, Weston Creek, ACT 2611, Australia

ABSTRACT

We have obtained deep ultraviolet imaging of the lensing cluster A1689 with the WFC3/UVIS camera onboard the *Hubble Space Telescope* in the F275W (30 orbits) and F336W (4 orbits) filters. These images are used to identify $z \sim 2$ star-forming galaxies via their Lyman break, in the same manner that galaxies are typically selected at $z \geqslant 3$. Because of the unprecedented depth of the images and the large magnification provided by the lensing cluster, we detect galaxies $100\times$ fainter than previous surveys at this redshift. After removing all multiple images, we have 58 galaxies in our sample in the range $-19.5 < M_{1500} < -13$ AB mag. Because the mass distribution of A1689 is well constrained, we are able to calculate the intrinsic sensitivity of the observations as a function of source plane position, allowing for accurate determinations of effective volume as a function of luminosity. We fit the faint-end slope of the luminosity function to be $\alpha = -1.74 \pm 0.08$, which is consistent with the values obtained for $2.5 < z < 6$. Notably, there is no turnover in the luminosity function down to $M_{1500} = -13$ AB mag. We fit the UV spectral slopes with photometry from existing *Hubble* optical imaging. The observed trend of increasingly redder slopes with luminosity at higher redshifts is observed in our sample, but with redder slopes at all luminosities and average reddening of $\langle E(B-V) \rangle = 0.15$ mag. We assume the stars in these galaxies are metal poor ($0.2\,Z_\odot$) compared to their brighter counterparts ($Z_\odot$), resulting in bluer assumed intrinsic UV slopes and larger derived values for dust extinction. The total UV luminosity density at $z \sim 2$ is $4.31^{+0.68}_{-0.60} \times 10^{26}$ erg s^{-1} Hz^{-1} Mpc^{-3}, more than 70% of which is emitted by galaxies in the luminosity range of our sample. Finally, we determine the global star formation rate density from UV-selected galaxies at $z \sim 2$ (assuming a constant dust extinction correction of 4.2 over all luminosities and a Kroupa initial mass function) of $0.148^{+0.023}_{-0.020}\,M_\odot$ yr^{-1} Mpc^{-3}, significantly higher than previous determinations because of the additional population of fainter galaxies and the larger dust correction factors.

1. INTRODUCTION

A primary goal of observational cosmology has been to obtain a complete census of star formation at all epochs (e.g., Madau et al. 1996; Lilly et al. 1996). One effective method of selecting star-forming galaxies is to identify a "Lyman break" in the ultraviolet (UV) continuum caused by Lyman line and continuum absorption from hydrogen in the stellar atmospheres, interstellar medium, and the intergalactic medium (IGM; Steidel et al. 1999). This technique was first used to select the star-forming galaxies as U-band "dropouts" at $z \sim 3$ (Steidel et al. 1999), and has since been widely adopted to select Lyman break galaxies (LBGs) at higher redshifts (e.g., Bunker et al. 2004, 2010; Sawicki & Thompson 2006; Yan et al. 2006, 2010; Bouwens et al. 2007, 2009; Reddy & Steidel 2009; Oesch et al. 2010b; Hathi et al. 2010).

Although the peak epoch of star formation is likely at lower redshifts ($1.5 < z < 3$, e.g., Ly et al. 2009; Reddy & Steidel

2009), it has been impossible to select galaxies at these redshifts via their Lyman break without imaging at wavelengths below the atmospheric limit, $\lambda < 3100$ Å. Other selection methods such as the BM/BX (Adelberger et al. 2004) and BzK (Daddi et al. 2004) criteria have been used, but unambiguous comparison with Lyman break selected galaxies at $z \geqslant 3$ is difficult because the selection effects are different.

The new Wide-Field Camera 3 (WFC3) on the *Hubble Space Telescope* (*HST*) has an ultraviolet/optical channel (UVIS) that increases survey efficiency (area $\times$ throughput) by more than an order of magnitude compared with WFPC2. With the first UV images in the Early Release Survey (ERS; Windhorst et al. 2011), star-forming galaxies were selected via the Lyman break technique at $1 < z < 3$ (Oesch et al. 2010a; Hathi et al. 2010). These studies were limited by the depth of the shallow UV imaging and could only detect galaxies with absolute UV magnitude (typically measured at 1500 Å, M_{1500}) brighter than -19 AB-mag, making it impossible to accurately constrain the faint-end slope of the UV luminosity function (LF).

Rest-frame UV light is a strong tracer of unobscured star formation, so the UV LF can be used to determine the relative contribution of faint and bright galaxies to the total star formation rate density (SFRD). The UV LF has been studied widely

---

at this active star forming era (Arnouts et al. 2005; Reddy & Steidel 2009; Hathi et al. 2010; Oesch et al. 2010a).

There are two difficulties in determining a complete census of star formation. First, the UV light emitted by bolometrically luminous galaxies is significantly attenuated by dust, which causes UV-selected samples to be incomplete at the bright end. However, these galaxies can be identified by their far-infrared emission (Reddy et al. 2006; Magnelli et al. 2011). Second, there may be a large population of faint star-forming galaxies beyond the detection limit of the deepest surveys (typically $M_{1500} < -18$ AB-mag).

This population of faint UV galaxies may contribute significantly to the global star formation density and the ionizing background (Nestor et al. 2013) at $z > 2$. Recent searches at $z = 3$ (Nestor et al. 2011) have revealed that faint star-forming galaxies on average have larger Lyman continuum escape fractions relative to the brighter galaxies. This result proves the importance of these feeble objects in maintaining the ionizing emissivity especially at the peak of star formation activity. In addition to the crucial role of the faint galaxies at lower redshifts, it is believed that low luminosity galaxies at $z > 7$ are likely the primary sources of ionizing photons that caused the reionization of the IGM (Kuhlen & Faucher-Giguère 2012; Robertson et al. 2013). Studying an analogous population at lower redshifts ($z \sim 2$) provides a clearer picture of ultra-faint populations at high redshifts.

One way to efficiently detect and study these faint galaxies is to use foreground massive systems as lenses to magnify background galaxies. This strong gravitational lensing conserves surface brightness while spreading out a galaxies' light over a larger area and magnifying it. Over the last decade, this has been used to study individual lensed galaxies in great detail (e.g., Pettini et al. 2002; Siana et al. 2008b, 2009; Stark et al. 2008; Jones et al. 2010; Yuan et al. 2013).

When using strong lensing to identify large numbers of faint galaxies, galaxy clusters are particularly useful as they highly magnify background galaxies over a large area (Narayan et al. 1984). The regions amplified by a higher factor have smaller source-plane area, so the benefit of magnification is offset by reduced sample volume. Therefore the total number of candidate galaxies behind a cluster could be either smaller or larger than a field survey of the same depth and area, due to the competition between these two variables. Determining the ratio of the total number of galaxies found by using cluster lensing relative to the field studies, depends on the effective slope of the LF (Broadhurst et al. 1995; Bouwens et al. 2009). If the effective slope of the LF, $-d \log \phi / d \log L$, is greater than unity then a survey behind a lensing cluster will find more objects than the same survey in the field. Lensing clusters have been used to identify very high redshift objects (e.g., Kneib et al. 2004; Egami et al. 2005; Stark et al. 2007; Bradley et al. 2008; Richard et al. 2008, 2011; Bouwens et al. 2009, 2012a; Zheng et al. 2012; Zitrin et al. 2012; Coe et al. 2013) because the luminosities probed are on the steep, bright end of the LF, resulting in larger samples than field surveys. Historically, surveys have not used lensing clusters to identify galaxies significantly fainter than L^* because it finds fewer galaxies. However, our primary concern is not the *number* of galaxies found, but the intrinsic *luminosity* of the galaxies. The average luminosity of galaxies found behind a lensing cluster will be significantly lower than surveys in the field. Because we are interested in finding galaxies that are undetected in our deepest field surveys, we chose to survey faint star-forming galaxies behind massive clusters. Once these

Table 1
WFC3/UVIS and ACS/WFC Magnitude Limits

Filter	F275W	F336W	F475W	F625W	F775W	F850LP
Magnitude limit[a]	28.7	27.90	28.55	28.29	28.17	27.80

Note. [a] 5σ limit in a $0\rlap{.}''2$ radius aperture.

ultra-faint galaxies are identified, the lensing will allow detailed study as they are highly magnified and the light is spread over many more resolution elements. This strategy of surveying large numbers of background galaxies with deep observations of lensing clusters will soon be adopted with deep *Hubble* imaging of the Frontier Fields beginning in Cycle 21.

In this paper we use the WFC3/UVIS channel to look for faint star-forming galaxies located behind the massive cluster A1689. This cluster has the most constrained cluster mass model due to the large number of confirmed multiply imaged systems (43), of which 24 have spectroscopic redshifts (Limousin et al. 2007; Coe et al. 2010). This mass model gives us a precise estimation of magnification factor over the total area. The high magnification area for this cluster is well-matched with the WFC3/UVIS field of view. A1689 has been observed extensively with *HST* in the optical with ACS/WFC (F475W, F625W, F775W, F814W, F850LP) and the near-IR with WFC3/IR (F105W, F125W, F140W, F160W), *Spitzer* IRAC and MIPS as well as *Herschel* PACS and SPIRE.

The outline of this paper is as follows. In Section 2, we describe the observations and data reduction. The selection technique is given in Section 3. In Section 4 we discuss the details of the completeness simulation as well as the Monte Carlo simulation used for IGM opacity. The redshift distribution of the sample is explained in this section. We explain the maximum likelihood method used for estimating the rest-frame UV LF parameters in Section 5. In Section 6 we determine the dust content of the selected LBGs. In Section 7, we compare our final results for the UV luminosity density and evolution of the faint-end slope and dust extinction with other results in the literature. We also briefly discuss about the effect of the intracluster dust. Finally, we present a short summary in Section 8.

All distances and volumes are in comoving coordinates. All magnitudes are given in the AB system (Oke & Gunn 1983). We assume $\Omega_M = 0.3$, $\Omega_\Lambda = 0.7$ and $H_0 = 70$ km s^{-1} Mpc^{-1}.

2. OBSERVATIONS

We used the WFC3 UVIS channel to obtain images in F275W (30 orbits) and F336W (4 orbits) as part of *HST* Program ID 12201 (PI: B. Siana) between 2010 December and 2011 March. We used long exposure times, half an orbit in length (1310s each) in order to minimize the total read noise, as this is the dominant source of noise in near-UV imaging with *Hubble*. The data were obtained in two orbit visits during which we performed the standard UVIS dither pattern, WFC3-UVIS-DITHER-BOX. Each dither pattern was offset up to $\pm 3''$ from the central pointing to place different pixels on the same objects and to fully cover the UVIS chip gap. The 5σ depths measured in a $0\rlap{.}''2$ radius aperture are given in Table 1.

In order to identify the LBGs at $z \sim 2$, we also used the existing *HST*/ACS images in optical bands (F475W, F625W, F775W, F850LP; PID 9289, PI: H. Ford). Table 1 shows the limiting magnitudes of these observations. The overlapping area
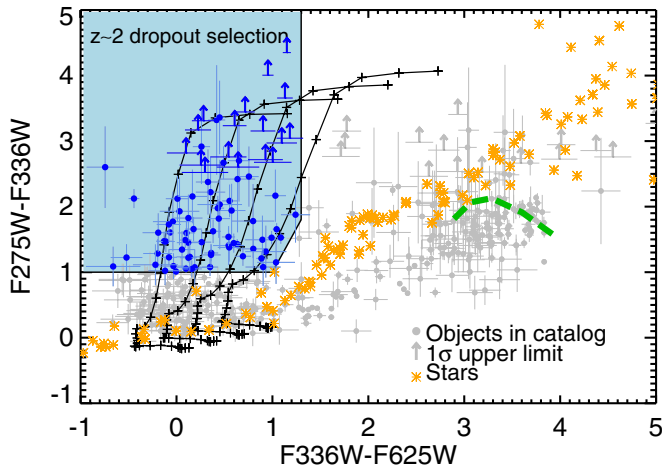
Figure 1. Color selection of $z \sim 2$ Lyman-break galaxies (F275W-dropouts). Gray dots are objects detected at greater than 5σ significance in F336W and F625W filters. Gray arrows represent 1σ upper limits. Black lines are tracks of star-forming galaxies that are dust obscured with $E(B-V) = \{0, 0.1, 0.2, 0.3\}$ (in magnitudes). Orange asterisks are stars from Pickles (1998). The blue shaded region is the region selected by the criteria given in Equation (2). The blue circles and blue arrows indicate our candidates. The green dashed line is the expected color track for lower redshift ($0.0 < z < 0.2$) elliptical galaxies (Coleman et al. 1980). A1689 is at $z = 0.18$. The large number of redder galaxies (in both colors) are primarily galaxies in A1689.

(A color version of this figure is available in the online journal.)

between the ACS/WFC and WFC3/UVIS fields of view, after subtracting the areas contaminated by the bright cluster galaxies, covers 6.56 arcmin^2 in the image plane.

2.1. Data Reduction

The calibrated, flat fielded WFC3/UVIS and ACS/WFC images were processed with *MultiDrizzle* (Koekemoer et al. 2003), part of the STSDAS/DITHER IRAF package (Tody 1986). The initial drizzled images were registered to Sloan Digital Sky Survey (SDSS) images in order to compute the shift file required for astrometric correction. Because each visit has a slightly different pointing and small differences in rotation and alignment, we make a shift file for each visit to project all the images to the same astrometric reference grid.

The F336W image was aligned with the SDSS g'-band image with a precision of $0\farcs1$, using unsaturated stars and compact objects. We chose to use the UVIS F336W image to align with SDSS because many of the stars were not saturated at these wavelengths and the galaxies were generally more compact, resulting in more precise alignment.

The other *HST* images were matched to F336W to achieve astrometric registration with the SDSS reference frame. The relative alignment of images was done with a precision of 0.1 pixels ($0\farcs004$) because of its importance in doing matched-aperture photometry in all filters. The shift files were created by running the *geomap* task in IRAF. These shift files were then used as input to re-run *MultiDrizzle*.

The input images to the *MultiDrizzle* software were drizzled onto separate undistorted output frames which were combined later into a median image. The median image was transformed back (blotted) to the original distorted images in order to make the cosmic ray masks. The final output is a registered, undistorted and cosmic ray-rejected image. We also set *MultiDrizzle* to produce an inverse variance weight image to be used for computing uncertainties in the photometry. In order to do matched-

aperture photometry for all wavelengths, we set the same output pixel sizes for WFC3/UVIS and ACS/WFC images to $0\farcs04$. We set the pixfrac, fraction by which the input pixels are shrunk before being drizzled, to 0.8 for ACS/WFC and 1 for WFC3/UVIS images since these pixfrac values were well matched to our output pixel scale.

The sources were detected in the ACS *B* band image (F475W) using *SExtractor* (Bertin & Arnouts 1996). The photometry was done by running *SExtractor* in dual image mode using the weight map RMS-MAP generated by *MultiDrizzle*. We used isophotal apertures with detection threshold 1.27σ and minimum area 16 pixels. We ran *SExtractor* with high and low values for the deblending minimum contrast parameter without changing other parameters in the *SExtractor* configuration file. We were able to detect very faint galaxies as separate objects in the catalog with very low DEBLEND-MINCONT = 0.005 and then add them to the other catalog produced with the larger DEBLEND-MINCONT = 0.13 parameter. This method is similar to hot and cold detections used in Rix et al. (2004). All of the isophotal magnitudes are given in AB magnitudes by using the WFC3 and ACS photometric zero points provided by STScI.

The output *SExtractor* uncertainties don't include the correlations between pixel counts that result from combing the input images with *MultiDrizzle*. Following Casertano et al. (2000) paper, the correction factor ($\sqrt{F_A}$) which is approximately the ratio of uncorrelated noise to correlated error from *SExtractor*, can be estimated as below:

$$\sqrt{F_A} = \begin{cases} \frac{s}{p}\left(1 - \frac{1}{3}\frac{s}{p}\right) & s < p \\ 1 - \frac{1}{3}\frac{p}{s} & s > p \end{cases} \quad (1)$$

where p is the pixfrac and s is the ratio of output pixel size to original pixel size.

We also supplemented our WFC3/UVIS and ACS/WFC images with WFC3/IR data, in order to compute the photometric redshifts. The higher resolution near-UV and optical images were convolved with Gaussians to degrade the resolution to that of the WFC3/IR images. The photometry was then measured using matched apertures in all images.

### 3. COLOR SELECTION AND SAMPLE

With our near-UV images we apply the Lyman break selection of $z \sim 2$ galaxies, allowing for direct comparison with $z \geqslant 3$ studies. The selection region is defined by the location of star-forming spectral energy distributions (SEDs) in color–color space. Our selection criteria, which are shown in Figure 1, were found by running Bruzual & Charlot (2003, hereafter BC03) models with constant star formation for 100 Myr, reddened by applying Calzetti attenuation curve (Calzetti et al. 2000) with $E(B-V) = \{0, 0.1, 0.2, 0.3\}$ (in magnitudes) and IGM obscuration from Madau (1995). The green dashed line is the track of lower redshift elliptical galaxies which is extended to $z = 0.2$, as A1689 is at $z = 0.18$.

Our color selection criteria for selecting the F275W dropouts are

$$\text{F275W} - \text{F336W} > 1$$
$$\text{F336W} - \text{F625W} < 1.3$$
$$\text{F275W} - \text{F336W} > 2.67(\text{F336W} - \text{F625W}) - 1.67$$
$$\text{S/N(F336W)} > 5, \quad \text{S/N(F625W)} > 5 \quad (2)$$

We found 84 candidates using these criteria. Four candidates were dismissed as they were fainter than the limiting magnitude
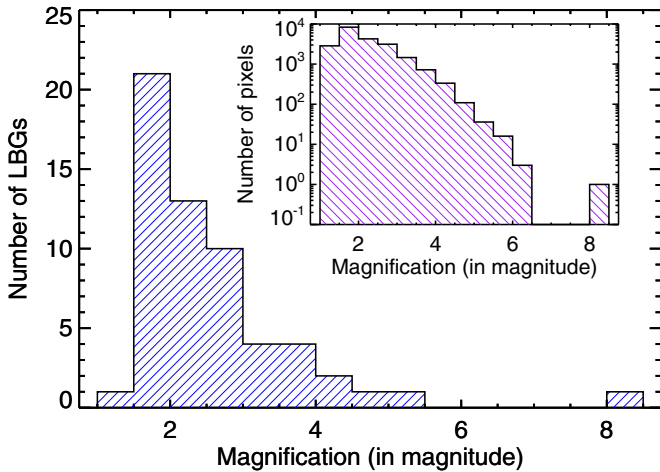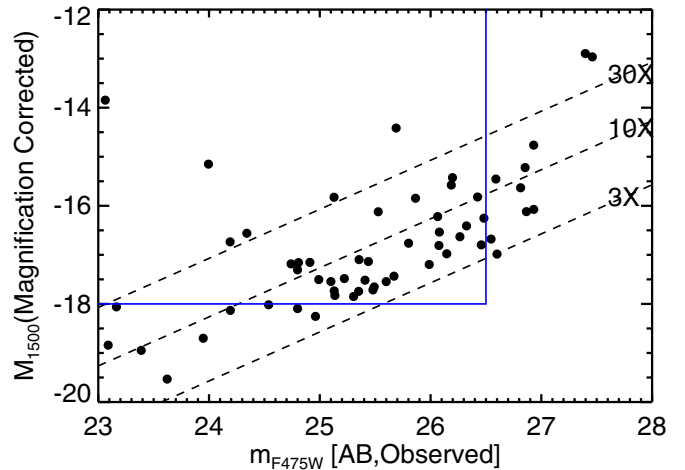
Figure 2. Magnification distribution function of Lyman-break galaxies. The magnification values are from the cluster lens model assuming the spectroscopic redshifts for 12 objects (see Section 4.3) and an average redshift of $z = 2$ (see Section 4.4) for the rest of the LBGs. The inset shows the distribution function of magnification values over all field of view pixels which are projected on the source plane at $z = 2$.

(A color version of this figure is available in the online journal.)

Figure 3. Intrinsic absolute magnitude, corrected for magnification, is plotted vs. observed B-band magnitude. There are 39 LBGs in the blue box which denotes galaxies that are both intrinsically faint ($M_{1500} > -18$) *and* bright enough ($B < 26.5$) for follow-up ground-based spectroscopy. Dashed lines show constant magnifications (3, 10, and 30 in flux density units).

(A color version of this figure is available in the online journal.)

in Table 1 (F336W = 27.9 mag and F625W = 28.29 mag). Because of the strong lensing phenomenon, many of the candidates in our sample are multiply imaged. In order to compute the LF, we must remove all but one of the multiple images from our catalog. We removed all of the previously known multiple images (12) except the brightest image in each system. In addition to these confirmed multiple images, the A1689 mass model predicts all of the possible counterimages for each object as a function of redshift. Using these predictions, we found eight new multiple images by performing a visual inspection considering the photometric redshift of each object (A. Dominguez et al. 2013, in preparation, also see Section 4.3). We removed two objects with photometric redshifts less than 1.3. Our final sample consists of 58 $z \sim 2$ LBG candidates (see Section 4).

The purity of our sample is quite high because of two main reasons. First, the possible contamination from other sources (e.g., stars) can be recognized easily, because these images are high resolution. Second, since these galaxies are UV dropouts, it is very unlikely to have any other break except Lyman break in the UV band. However the contamination from similar galaxies (LBGs) at slightly either higher or lower redshifts, is not negligible. We account for these possible contaminants in our completeness simulation (see Section 4.3).

The selected LBGs have observed B-band magnitude down to $m_{F475W} < 27.5$ mag, but are intrinsically fainter as they are all highly magnified. The lensing cluster mass model estimates the magnification value at each point of the image as a function of redshift. The magnification of each LBG was measured by assuming the spectroscopic redshifts for 12 out of 58 LBGs (see Section 4.3) and an average of $z = 2$ (see Section 4) for the rest of the sample. Figure 2 shows the distribution of magnification in magnitude units for all the UV-dropout galaxies. The fluxes are on average magnified by a factor of 10 (2.5 mag) and for some galaxies the magnification becomes very large (up to 8 mag). The distribution of magnification over the whole field of view in the source plane at $z = 2$ is given in Figure 2 (inset), which shows all the pixels in this area are magnified by at least one magnitude.

Due to the large magnifications, the intrinsic absolute magnitudes measured at rest frame 1500 Å, M_{1500}, probed in this study go down to very faint magnitudes ($M_{1500} < -13$ mag), about 100 times fainter than previous studies ($M_{1500} < -18$ mag) at the same redshift (Reddy & Steidel 2009; Hathi et al. 2010; Oesch et al. 2010a; Sawicki & Thompson 2006). The intrinsic absolute magnitudes corrected for magnification (M_{1500}) versus observed B-band magnitudes (F475W) are plotted in Figure 3. The dashed lines represent the fixed magnifications of 3, 10, and 30 in flux density units. There are 39 galaxies within the blue box which are both intrinsically very faint ($M_{1500} > -18$ mag) and bright enough ($m_{F475W} < 26.5$ mag) due to magnification to get ground-based spectroscopy in the rest-frame UV and optical bands.

4. COMPLETENESS

The completeness correction factor $C(z, m, \mu)$ is the probability that a galaxy at redshift, z, with intrinsic apparent magnitude, m, and magnification, μ, will be detected in our magnitude limited sample and also satisfy our color selection criteria. The completeness is affected by several factors: intrinsic luminosity, dust extinction, magnification, size and IGM opacity. In the subsequent subsections, we will describe how these quantities vary and how these variations are implemented in the completeness simulations.

4.1. Simulating the Faint Galaxies

We used BC03 models to generate a template spectrum by assuming a Chabrier initial mass function (IMF), constant star formation rate (SFR), 0.2 $Z_{\odot}$ metallicity, and an age of 100 Myr. Both Salpeter (Salpeter 1955) and Chabrier (Chabrier 2003) IMFs roughly follow the same power law for stars with $M > 1\,M_{\odot}$. However at smaller masses there are significant differences. This results in different stellar mass determinations, while having little effect on the UV SEDs.

We choose to use a somewhat younger, 100 Myr, stellar population (Haberzettl et al. 2012; Hathi et al. 2013) than is typically used at these redshifts for star forming galaxies (~300 Myr, e.g., Shapley et al. 2005; Reddy et al. 2008) as the

Table 2
Parameters of Column Density Distribution and Redshift Distribution of Intervening Absorbers

Name	$\log(N_H)$	k [a]	N_0 [b]	γ [b]	b [c] (km s^{-1})	Redshift [b]
Lyman-α forest	12–14	1.67	50.12	1.18	30	$1.9 \leqslant z$
			62.52	0.78	30	$z < 1.9$
	14–17.5	1.67	6.02	2.47	30	$1.9 \leqslant z$
			16.98	1.66	30	$0.7 \leqslant z < 1.9$
			35.4	0.13	30	$z < 0.7$
Lyman limit system (LLS)	17.5–20.3	1.07	0.17	1.33	70	$z < 2.6$
Damped Lyman-α system (DLA)	20.3–21.5	1.71	0.04	1.27	70	$z < 5$
	21.5–22	11.1	0.04	1.27	70	$z < 5$

Notes.
[a] The values are taken from O'Meara et al. (2013).
[b] The column density distribution parameters N_0 and γ are from Janknecht et al. (2006), Ribaudo et al. (2011), and Rao et al. (2006) for Lyman-α forests, LLSs, and DLAs, respectively.
[c] The doppler parameter values are from Kim et al. (1997) and Moller & Jakobsen (1990).

target galaxies are typically smaller and have shorter dynamical timescales than their more massive counterparts. The SEDs don't change significantly for stellar ages between 100 Myr and 300 Myr (Leitherer et al. 1999), therefore our assumption for the age does not have a large effect on our main results (see Section 6). We will present the ages from SED fitting in a future paper (A. Dominguez et al. 2013, in preparation). The star formation histories are undoubtedly more complicated than the assumed constant rate, but the UV SED reacts slowly (on timescales of 50 Myr) to sudden changes (Leitherer et al. 1999) and smooths out the effects of small timescale star formation events.

Our galaxies have low stellar masses ($7 < \log(M/M_\odot) < 9$; A. Dominguez et al. 2013, in preparation). Applying the mass-metallicity relation at these redshifts (Erb et al. 2006; Fynbo et al. 2008; Belli et al. 2013; Yuan et al. 2013) to these galaxies gives a lower value than is typically assumed in similar studies which are based on brighter galaxies (0.2 versus 1 $Z_\odot$).

The Calzetti attenuation curve (Calzetti et al. 2000) was used for the dust extinction by assuming a Gaussian distribution for $E(B-V)$ centered at 0.14 mag (Steidel et al. 1999; Hathi et al. 2013) with a standard deviation of 0.1.

We also estimated the completeness for the typical stellar population assumptions (300 Myr and 1 $Z_\odot$) and again a Gaussian distribution for $E(B-V)$ centered at a value lower than 0.14 mag (0.05 mag, see Section 6) to see if varying the input stellar population parameters changes the results significantly. Our completeness determinations are robust against these initial considerations.

4.2. Monte Carlo Simulation: IGM Opacity

UV (both Lyman emission line and continuum) photons are absorbed by neutral hydrogen clouds located along the line-of-sight to any galaxy. These intervening absorbers are classified in three groups based on their hydrogen column densities : Lyman-α forest (10^{12} cm$^{-2} < N_H < 10^{17.5}$ cm^{-2}), Lyman limit systems (LLSs, $10^{17.5}$ cm$^{-2} < N_H < 10^{20.3}$ cm^{-2}) and damped Lyman-α systems (DLAs, $N_H > 10^{20.3}$ cm^{-2}). The column density distribution of these absorption clouds is given as

$$\frac{df}{dN_H} \propto N_H^{-k} \qquad (3)$$

and their number density distribution (number per unit redshift) changes as a power law with redshift.

$$N(z) = N_0(1+z)^\gamma \qquad (4)$$

Where N_0 is the number of absorbers per unit redshift at present time ($z = 0$). The values we have adopted (from the literature) for k, N_0 and γ are given in Table 2 (Janknecht et al. 2006; Rao et al. 2006; Ribaudo et al. 2011; O'Meara et al. 2013).

The IGM opacity at each line-of-sight is computed by running a Monte Carlo simulation. A complete description of this simulation is presented in Siana et al. (2008a). Here we briefly summarize how the IGM absorption code works.

We randomly vary the number of absorbers along the line of sight to each galaxy by sampling from a Poisson distribution with the expectation value $\langle N \rangle$.

$$\langle N \rangle = \int_0^{z_{\rm galaxy}} N(z)dz \qquad (5)$$

We then select a column density and redshift for the absorber from the distributions in Equations (4) and (5), respectively. We determine the Voigt profile with doppler parameters given in Table 2, for the first twenty Lyman lines for each absorber. Finally, the IGM transmission for non-ionizing UV wavelengths at each line of sight is derived by adding the optical depths of randomly selected absorbers. We also incorporate the opacity to Lyman continuum photons using a photo-ionization cross section of $\sigma = 6.3 \times 10^{-18}$ cm^2 and decreasing as λ^3 for $\lambda < 912$ Å. We generated 1000 lines-of-sight at each redshift in steps of $\Delta z = 0.1$ over the required redshift range for the completeness simulation ($1 < z < 3$, see Section 4.3).

4.3. Simulation: Incompleteness Correction

We created a 3-D grid to compute the completeness as a function of redshift z, magnitude m and magnification μ. For each point in this 3-D space, the SED generated by BC03 was redshifted, magnified and then attenuated by the IGM for 300 randomly selected line-of-sights. At each line-of-sight, the dust attenuation is sampled randomly from the Gaussian distribution mentioned above.

As was mentioned before (see Section 3), the primary contaminants in our sample are similar galaxies (LBGs) at slightly higher or lower redshifts. The photometric uncertainties can scatter the galaxies both into and out of the selection region.
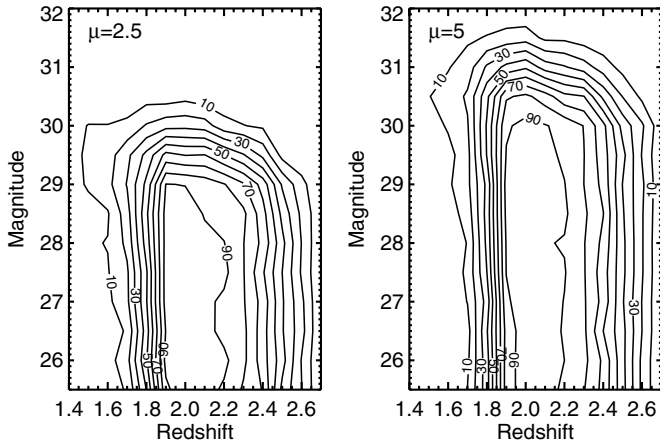
Figure 4. Completeness contours as a function of intrinsic F475W apparent magnitude and redshifts. The contours are plotted for two values of magnification, $\mu = 2.5$ mag (left, the typical magnification) and $\mu = 5$ mag (right, an extreme magnification in our sample).

Adding these to the completeness simulation effectively broadens the redshift distribution of our sample. The photometric uncertainties are assumed to have a Gaussian distribution with $\sigma \propto \sqrt{area}$ (assuming a constant instrumental noise over the object's area). We assume a normal distribution for the galaxy sizes centered at 0.7 kpc (Law et al. 2012) with $\sigma = 0.2$ kpc. At each line-of-sight, the randomly selected area is magnified by the magnification factor.

There is another important factor which can affect our completeness simulation. Charge transfer inefficiency (CTI) causes some signal to be lost during the readout. The CTI depends on the flux density of the object, sky background, the distance on the detector between the object and the readout amplifier and the time of the observation (e.g., as the CTI worsens with time, Baggett et al. 2012; Teplitz et al. 2013). This problem is more significant for images with very low background similar to our images in the F275W band ($\sim 0.5\ e^-$, Teplitz et al. 2013). Therefore CTI associated charge loses would make some galaxies fainter in the F275W band and push them inside the color selection region. We consider this issue in our completeness computations based on the analysis done in Noeske et al. (2012). The CTI is estimated as follows:

$$m_{(corr)} = m_{(uncorr)} - S\frac{Y}{2048} \qquad (6)$$

where Y is the distance in rows between the simulated galaxy and readout amplifier. For each line-of-sight, Y is randomly selected from a uniform distribution. S is a 2nd degree polynomial function of flux and observation date. More information related to the estimation of CTI is given in Noeske et al. (2012). The CTI corrections are small for most of the F275W-detected objects (<0.1 mag), therefore they do not have a significant effect on the completeness results. In Section 4.5, we discuss about the possibility that CTI causes galaxies to be undetected in the F275W filter.

Therefore, at each point in the 3D grid (z, m, μ), we simulate 300 galaxies at different lines of sight with different reddening, distance from readout amplifier and noise (size) selected from the related distributions mentioned above. The completeness was computed by counting the fraction of galaxies that satisfy the same selection criteria as the real observed objects (Equation (2)).
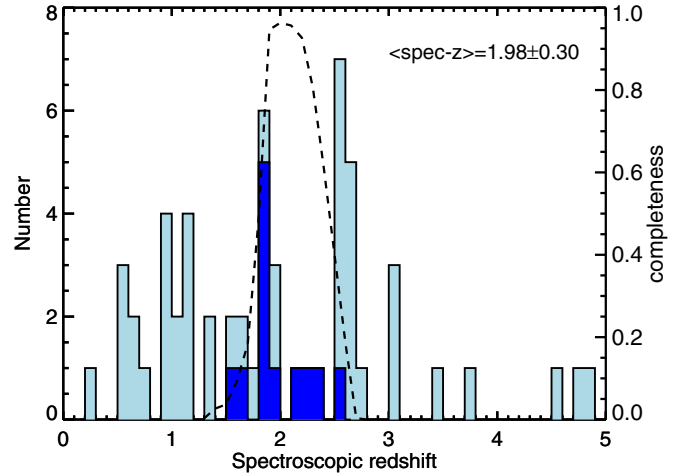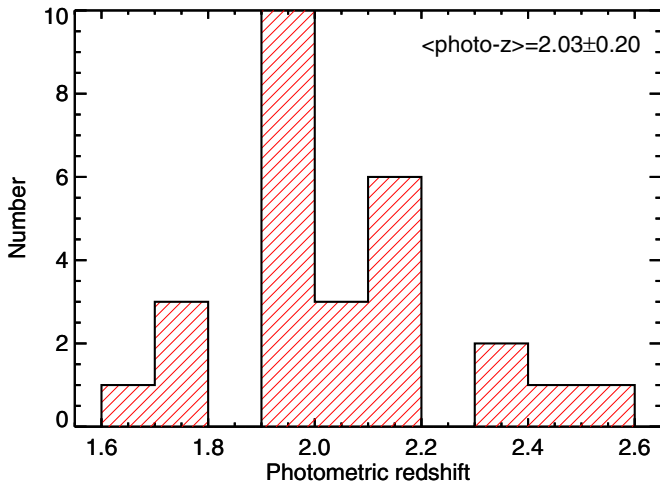

Figure 5. Spectroscopic redshift distribution. The redshift histogram for galaxies with spectroscopic redshift is shown in light blue. The dark blue histogram shows the spectroscopic redshift distribution of 12 galaxies selected as $z \sim 2$ LBGs in our image. We recovered 75% of galaxies (9 of 12) in the range $1.8 < z < 2.4$ where we should have high selection completeness. A few over densities are evident at $z \sim 1.83$ and $z \sim 2.54$. The right-hand axis shows the completeness values from the simulation. The dashed line shows the simulated completeness distribution over the redshift for a galaxy with typical intrinsic apparent magnitude ($m_{F475W} = 27.5$) and magnification ($\mu = 2.5$ mag).

(A color version of this figure is available in the online journal.)

The completeness contours are given in Figure 4. The contours are plotted for two different values of magnification, $\mu = 2.5$ and $\mu = 5$ in units of magnitude which are the average and maximum predicted magnifications by the mass model for the LBG candidates in the sample. The figure indicates that the completeness as a function of absolute magnitude is obviously dependent upon the magnification. The color selection criteria represented in Section 3 is more than 90% complete between $1.9 < z < 2.1$.

As a test of the completeness simulation, we compare to the completeness of our selection of LBGs from a parent sample of galaxies with spectroscopic redshifts. The spectroscopic redshifts are discussed in J. Richard et al. (2013, in preparation) and D. Stark et al. (2013, in preparation). These spectroscopic campaigns have targeted primarily galaxies with high magnification (arcs) so many of the galaxies are intrinsically faint. In the core of the lensing cluster, we have targeted multiply imaged systems. Because the multiple systems are important for modeling the mass distribution of the cluster, they were targeted down to very faint magnitudes ($m_{475} \sim 27.0$). Therefore the final spectroscopic sample is less biased toward luminous galaxies than it would be in a blank field without magnification. In the outskirts of the cluster, where the magnification is lower, spectra were obtained for a variety of galaxies.

Figure 5 shows the redshift distribution of all 57 objects with spectroscopic redshifts in the field together with the subsample selected as LBGs. A few over densities are seen at $z = 1.83$ and $z = 2.54$. The dashed line is the completeness distribution for a galaxy with typical intrinsic apparent magnitude ($m_{F475W} = 27.5$) and magnification ($\mu = 2.5$ mag). We detected 75% of the galaxies in the redshift range, ($1.8 < z < 2.4$), consistent with our completeness calculations. The simulated completeness values are given at right-hand axis. The tail in the dashed line seen at lower redshifts shows the contamination from lower redshift galaxies (see Section 3). This effect slightly broadens the redshift distribution of our sample, and is accounted for in the completeness simulation.

Figure 6. Photometric redshift distribution from SED fitting to eight *HST* bands spanning UV, optical, and near-IR wavelengths. The photometric redshift uncertainty is $\Delta = |(z_{phot} - z_{spec})|/(1 + z_{spec}) = 0.02$ when comparing to the six galaxies in the sample with spectroscopic redshifts.

(A color version of this figure is available in the online journal.)

We see that the observed completeness, ratio of these two spectroscopic redshift histograms at each bin, is in good agreement with the corresponding simulated completeness value (dashed line). Predicting a high value of simulated completeness in the redshift bin $1.9 < z < 2$, we might expect to have more than one LBG out of three at this redshift interval. One of the objects was not selected because it is not a 5σ detection in F336W.

4.4. Redshift Distribution

In order to determine luminosities and magnifications, we need to know the mean redshift of galaxies in our sample (and its dispersion). From our completeness function (Figure 4), if we assume that there is no strong evolution of number density with redshift, we would expect the average redshift of the sample to be between $2.0 \lesssim z \lesssim 2.1$. Given the unknown number density evolution and the possibility of structure along the line-of-sight, we determine the average redshift of the sample from both the spectroscopic and photometric redshifts.

From the 12 galaxies with spectroscopic redshift, we obtain an average redshift, $\langle z \rangle = 1.98$ with a dispersion of $\sigma_z = 0.30$, in agreement with the completeness simulations.

To obtain a larger sample of redshifts, we calculated photometric redshifts for a sample of 26 galaxies that lie within the WFC3/IR image footprint. These photometric redshifts should be more precise because of the addition of the near-IR data, which span the Balmer/4000 Å break at $z \sim 2$. We used the EAZY code (Brammer et al. 2008) to determine photometric redshifts of our eight *HST* band (UV, optical and IR) catalogs. We compare the photometric and spectroscopic redshifts (6 in this sample) to determine the fractional redshift error, $\Delta = |(z_{phot} - z_{spec})|/(1 + z_{spec}) = 0.02$. The dispersion of the photometric versus the spectroscopic redshifts shows that there is no bias in our photometric redshift estimates. Figure 6 shows the estimated photometric redshift distribution of the 26 candidates that have near-IR photometry. The mean of the photometric redshift distribution is $z = 2.03$ with a dispersion of $\sigma_z = 0.20$, in agreement with what we expect from the completeness simulation.

Given the average and dispersion of our spectroscopic and photometric redshifts, we assume an average redshift $\langle z \rangle = 2.00$ with a dispersion of $\sigma_z = 0.25$ for LBGs without spectroscopic redshifts. For comparison, the studies of Oesch et al. (2010a) and Hathi et al. (2010), using similarly selected samples, assumed average redshifts of 1.9 and 2.1, respectively.

4.5. F275W Non-detections and CTI

Our completeness simulations account for the small corrections to F275W magnitudes from CTI. However, one concern is that very faint F275W fluxes near the detection limit will be lost completely due to CTI. Of the final sample of 58 sources, 11 are undetected in F275W. Most of these 11 galaxies are bright in F336W and would have bright F275W magnitudes if they were blue enough to lie outside of our selection window. Therefore, CTI cannot be responsible for the non-detection in F275W. However, there are five galaxies with F336W > 27.0 mag, meaning that the F275W magnitude of an LBG would have to be fainter than F275W > 28.0 mag to be selected as an LBG. For these galaxies, CTI can cause a non-detection if the galaxy is far from the readout amplifier. The galaxies are 422, 1104, 1141, 1604, and 1620 pixels from the read amplifier. It is possible that a few of the galaxies that are far from the amplifier (>1000 pixels) may be in our sample because of CTI issues. We note however that these galaxies span a range in intrinsic UV magnitudes (-16.98 mag $< M_{1500} < 15.22$ mag) where there are many galaxies per bin. Therefore, even in the worst case scenario that all four of these galaxies are low-z interlopers, the CTI concerns will not significantly affect the conclusions of this paper.

We are using two orbits of our cycle-20 program to test the effects of CTI in our F275W image and will refine our selection in the future.

5. LUMINOSITY FUNCTION

The UV LF at rest-frame 1500 Å is measured by using the spectroscopic redshifts for 12 out of 58 dropout candidates and assuming a mean redshift of 2.0 for the rest of the objects. The absolute magnitudes are computed at 1500 Å by using the apparent magnitude at F475W as below:

$$M_{1500} = m_{F475W} + \mu - 5\log(d_L/10\,pc) + 2.5\log(1 + z) \quad (7)$$

Where μ is the magnification in magnitudes predicted by the lens model. The luminosity distribution of galaxies can be parameterized by a Schechter function which has three parameters: faint end slope (α), characteristic luminosity (L^*) and normalization coefficient (ϕ^*).

The accurate approach to fitting the LF is the maximum likelihood method (Sandage et al. 1979) using the individual galaxies and their associated effective volumes. The main advantage of this approach is in using the unbinned data. Fits to binned data are imprecise as the choice of bin size and center effects the results. Furthermore, the completeness and the effective volume can change significantly from one side of the bin to the other.

In addition to using our data in the maximum likelihood fitting process, we used the individual data points from Oesch et al. (2010a) $z = 1.9$ sample as well. Their sample includes the rare, bright galaxies which are not present in our small survey volume, but are necessary to constrain L^*.

Table 3
UV Luminosity Function Parameters

Method	z	α	M^*	$\log_{10}\phi^*$ (Mpc^{-3} mag^{-1})
Maximum likelihood[a]	2.0	-1.74 ± 0.08	-20.01 ± 0.24	-2.54 ± 0.15

Note. [a] Maximum likelihood fit to the whole sample including both this work (A1689) and Oesch et al. (2010a).

The probability that a galaxy with absolute magnitude M_i is detected in our magnitude limited sample is

$$P(M_i) = \frac{\phi(M_i)V_{\text{eff}}(M_i)}{\int_{-\infty}^{M_{\text{limit}}} \phi(M)V_{\text{eff}}(M)dM} \qquad (8)$$

Where ϕ is the parametric LF and M_{limit} is the faintest intrinsic absolute magnitude in the sample. V_{eff} is the effective comoving volume in which a galaxy with magnitude M can be found. The effective volume associated with each galaxy in our sample is derived by taking incompleteness into account,

$$V_{\text{eff}} = \int_{\mu > \mu_0} \int_0^\infty \frac{dV_{\text{com}}}{dz d\Omega} C(z, m, \mu)\Omega(\mu)dz d\mu \qquad (9)$$

where V_{com} and Ω are the comoving volume and solid angle, respectively. $\Omega(\mu)$ is an area in the source plane that is magnified by a factor of μ. Due to the distortion generated by gravitational lensing, the total effective area in the source plane is 0.37 arcmin^2 at $z \sim 2$ which is significantly smaller than the total area in the image plane. μ_0 is the minimum magnification needed for detecting an object with magnitude M relative to the magnitude limit. $C(z, m, \mu)$ is the completeness computed in Section 4.

The best fit to the LF was found by maximizing the joint likelihood $\mathcal{L}$, which is the product of individual probabilities taken at all (unbinned) data points of the sample.

$$\mathcal{L} = \prod_{i=1}^N P(M_i) \qquad (10)$$

where N is the total number of objects in both samples (A1689 and Oesch et al. 2010a). In this method the normalization coefficient is canceled out so it must be estimated separately from the number counts.

$$\phi^* = \frac{N}{\int_{M_1}^{M_2} \phi(M)V_{\text{eff}}(M)dM} \qquad (11)$$

Where M_1 and M_2 represent the brightest and faintest candidates in the sample, respectively.

There are three sources of uncertainty in the determination of the intrinsic absolute magnitudes for *our* sample. First, we do not know the redshift of most galaxies (except those with spectroscopic redshifts, Section 4.3), so the conversion from apparent to absolute magnitude is uncertain. We used the completeness computations given in Section 4.3 (Figure 4) to estimate the standard deviation of the redshift distribution, $\Delta z = 0.25$, which is consistent with the photometric and spectroscopic redshift distributions. Using this $\Delta z = 0.25$, we derive an absolute magnitude uncertainty of $\sigma_z = 0.24$ mag. Second, again due to the unknown source redshift, the magnification estimate from the mass model is uncertain. Using the same redshift uncertainty, $\Delta z = 0.25$, we find a $\sigma_\mu = 0.10$ mag. The third uncertainty is from the A1689 lens model, σ_{model}. Limousin et al.

(2007) has used a parametric method to describe the mass distribution of A1689. In this parametric approach, they utilize the observational constraints (multiply imaged systems) to optimize the parameters (minimum χ^2) of the lens model (see Limousin et al. 2007, Equation (3)). We computed the lens model uncertainty by producing a series of models through sampling the parameter space around a similar χ^2 as the best model. We used a Bayesian Markov Chain Monte Carlo sampler in Lenstool (Jullo et al. 2007). The mean and the median values of this uncertainty are 0.08 and 0.04 mag, respectively.

The total absolute magnitude uncertainty, σ, for the objects with spectroscopic redshift is simply σ_{model}. Because the effect of luminosity distance and magnification when varying the redshift are correlated, they change the absolute magnitude in the same way. Therefore, σ for the rest of the objects is computed by summing the first two uncertainties, σ_z and σ_μ, and then adding the lensing model uncertainty in quadrature. This uncertainty in the absolute magnitude measurement is incorporated into the analysis by marginalizing over the probability distribution of each object's magnitude. The conditional probability that a galaxy with magnitude M_i is in the sample, given the total uncertainty (σ_i) can be estimated through marginalization,

$$P(M_i|\alpha, \sigma_i) = \int_{-\infty}^\infty P(M_i|\mu, \alpha, \sigma_i)P(\mu|\sigma_i)d\mu \qquad (12)$$

where $P(M_i \mid \mu, \alpha, \sigma_i)$ is the Schechter function at magnitude M_i. The probability of each magnification measurement is given by a normal distribution,

$$P(\mu|\sigma_i) = \frac{1}{\sqrt{2\pi}\sigma_i} e^{\frac{-(\mu-\mu_i)^2}{2\sigma_i^2}} \qquad (13)$$

where the mean value, μ_i, is the magnification assigned to each candidate by using the ratio of source and image plane luminosities from the A1689 mass model (Limousin et al. 2007) and assuming an average redshift $z = 2$ for all of the objects.

The best-fit UV LF parameters are tabulated in Table 3. Figure 7 shows the best-fit LF derived from the maximum likelihood method along with previous determinations (Reddy & Steidel 2009; Hathi et al. 2010; Oesch et al. 2010a; Sawicki 2012). The inset shows the 68% and 95% likelihood contours of the Schechter parameters. In order to display our data better (black filled circles in Figure 7), we defined the absolute magnitude bins and then calculated the LF over these bins as below:

$$\phi(M_i)dM_i = \frac{N_i}{V_{\text{eff}}(M_i)} \qquad (14)$$

Where N_i is the number of galaxies in magnitude bin i and V_{eff} is the effective comoving volume computed in Equation (9). We emphasize that we fit to individual points and not the binned data.

We examined the convergence of the completeness simulation by splitting the simulation in half (150 line-of-sights each). We then re-ran the simulation code and re-fit the LF parameters
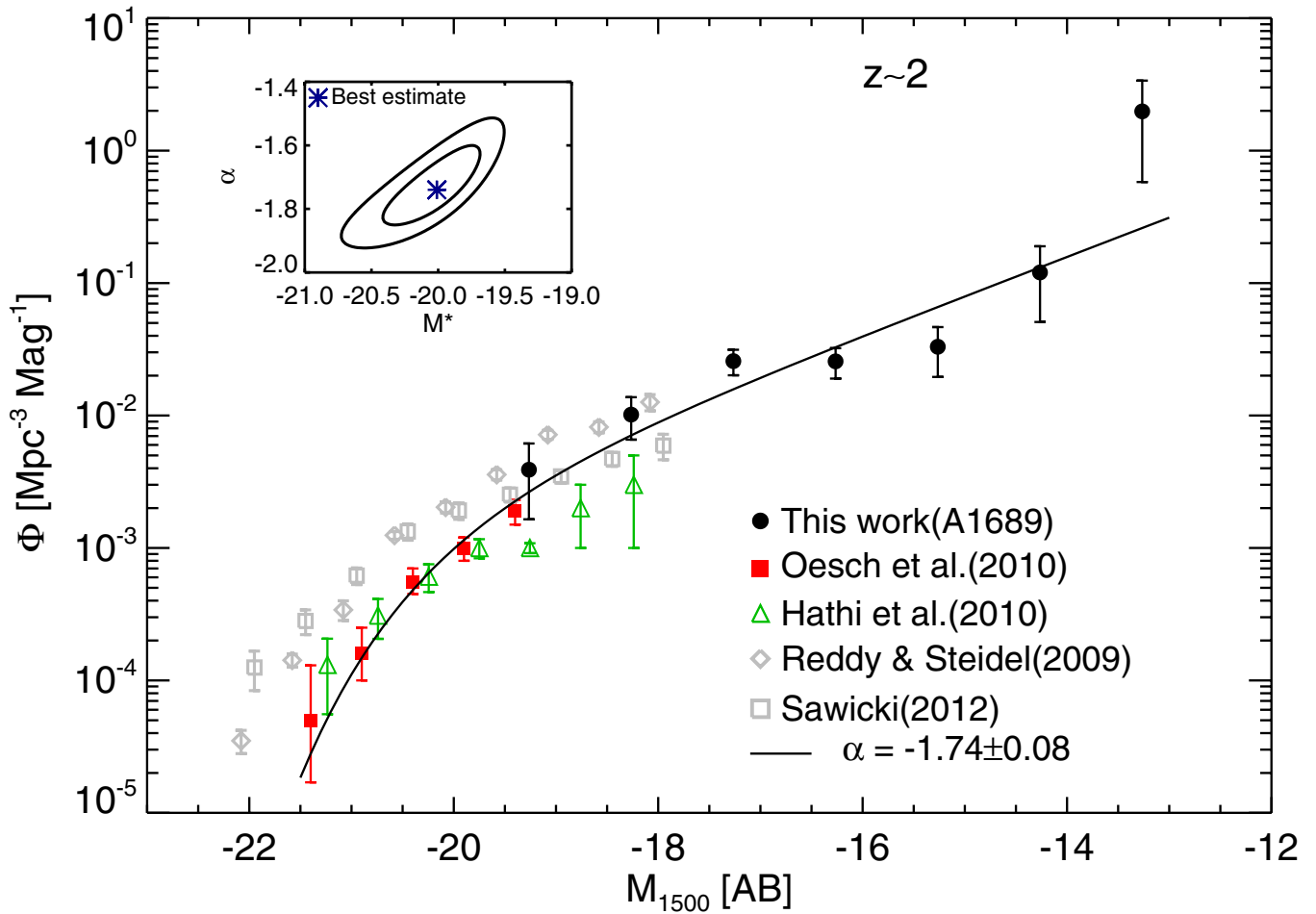
Figure 7. UV luminosity function at $z \sim 2$. The black circles are our binned luminosity function values computed by using Equation (14). The red filled squares and the green open triangles are the LFs from Oesch et al. (2010a) and Hathi et al. (2010), respectively, which are selected in a similar manner to our sample and are at the same redshift ($z \sim 2$). Gray open diamonds and gray open squares are the LFs at slightly higher redshift ($z \sim 2.3$) from Reddy & Steidel (2009) and Sawicki (2012), respectively. The black solid line is the best unbinned maximum likelihood fit to the whole sample of our data and Oesch et al. (2010a). The inset shows the 68% (1σ) and 95% (2σ) confidence contours of the Schechter parameters.

(A color version of this figure is available in the online journal.)

using the maximum likelihood approach. The difference between the new estimates of each Schechter parameter and what we found before, is less than 4% of the previously determined uncertainty of each parameter. We conclude that our simulation has converged for the adopted number of line-of-sights (300, see Section 4).

5.1. Cosmic Variance

The cosmic variance uncertainty σ_{CV} in the galaxy number counts can be estimated through the effective volume of the survey, the survey geometry, and an estimate of the typical clustering bias of the discovered sources. In what follows, we compute the cosmic variance uncertainty for the lensed field.

The effective volume of our survey has been calculated using the methods described in Section 5. We use these effective volumes and the selection function of the survey with redshift to determine the root-mean-squared (RMS) density fluctuations σ_ρ expected in our survey volume given its pencil beam geometry, following the methodology of Robertson (2010). We find these density fluctuations to be $\sigma_\rho \approx 0.1$, which is determined largely by the line-of-sight extent of the pencil beam survey (the comoving radial distance over the redshift range $1.75 \leqslant z \leqslant 2.35$ where our selection is efficient) and the linear growth factor $D(z \sim 2) \approx 0.4$ (Robertson et al. 2013).

To determine the cosmic variance uncertainty in the galaxy counts, we perform a simple abundance matching calculation (e.g., Conroy et al. 2006; Conroy & Wechsler 2009) assigning galaxies in our survey approximate halo masses and clustering bias based on their volume abundances. For galaxies in our survey, the estimated bias is $b \sim 1.2$–2.6, providing a cosmic variance uncertainty of $\sigma_{CV} \approx 0.12$–0.25 (e.g., Robertson 2010), comparable to our fractional Poisson uncertainty $1/\sqrt{N} \approx 0.13$. We therefore expect that cosmic variance does not strongly influence the LF results. Further, since cosmic variance instills a covariance in the galaxy number counts as a function of luminosity (see, e.g., Robertson 2010), if our survey probes either an over- or under-dense region compared to the cosmic mean the covariance in the counts should have little effect on the intrinsic shape of the LF (especially at faint magnitudes where the galaxies are nearly unbiased tracers of the dark matter). Our faint-end slope determination is therefore expected to be robust against systematic considerations owing to cosmic variance uncertainties.

6. UV SPECTRAL SLOPE

The UV continuum of galaxies can be approximated as a power law, $f_\lambda \propto \lambda^\beta$ (Calzetti et al. 1994). The UV spectral
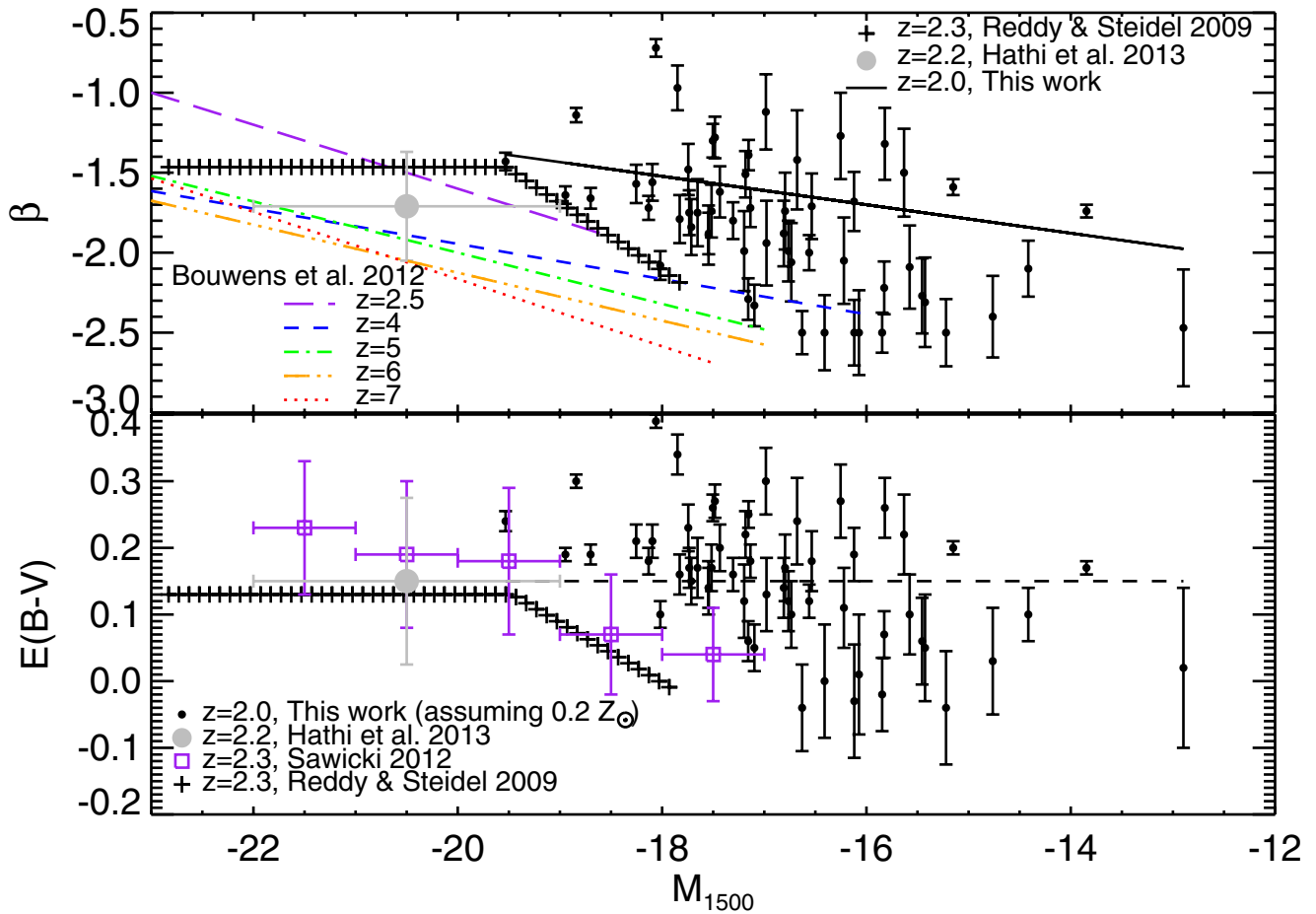
Figure 8. Upper panel: UV spectral slope as a function of absolute UV magnitude at 1500 Å. The black solid line is the best linear fit to our individual data. The line made of plus symbols is from Reddy & Steidel (2009). The purple long dashed, blue dashed, green dot-dash, orange dot-dot-dash, and red dotted lines are the best linear fit for redshifts 2.5, 4, 5, 6, and 7, respectively, from Bouwens et al. (2012b). The gray point shows the average and dispersion of values measured by Hathi et al. (2013) at $z \sim 2$. Lower panel: $E(B-V)$ as a function of absolute UV magnitude at 1500 Å. Our reddening values (black filled circles) are computed assuming 0.2 $Z_{\odot}$, but the other $E(B-V)$ values have been found assuming 1 $Z_{\odot}$. The purple open squares are from Sawicki (2012). The rest of the symbols are the same as those in the upper panel. The dashed line is an average of our $E(B-V)$ values and *not* a fit to our data.

(A color version of this figure is available in the online journal.)

slope, β, of each galaxy in our sample was estimated by making fake power law spectra over a wide range of β values and multiplying these spectra with the filter curves. We then have a one-to-one map of the observed color to the spectral slope. We use the F475W and F625W filters to measure the UV spectral slope as they correspond to rest-frame wavelengths of $\sim$1580 Å and $\sim$2080 Å respectively, at $z \sim 2$. The uncertainty of the β estimate for each individual object was derived by using the photometric uncertainties in both the F475W and F625W filters.

The $E(B-V)$ values, which have a one to one relation with UV spectral slopes, are obtained based on the comparison of observed UV colors with the colors predicted from the stellar population synthesis model (BC03) and reddened with a Calzetti attenuation curve (Calzetti et al. 2000). We used the realistic assumptions for the age (100 Myr) and the metallicity (0.2 $Z_{\odot}$) of these compact faint galaxies (see Section 4.1). In order to compare the importance of the age and metallicity in the color excess measurements, we also estimated the $E(B-V)$ values considering the more typical assumptions for these two quantities (1 $Z_{\odot}$ & 300 Myr). We present the color excess $E(B-V)$ distributions for three sets of age and metallicity assumptions, [(0.2 $Z_{\odot}$ & 100 Myr), (0.2 $Z_{\odot}$ & 300 Myr), (1 $Z_{\odot}$ & 100 Myr)] in Figure 10. The black histogram shows the distribution resulting from the realistic assumptions for the age

and metallicity ($Z = 0.2\, Z_{\odot}$ and age = 100 Myr). We see that varying the assumed metallicity (right panel, blue distribution) dominates the effect on the determined reddening distribution, whereas changing the assumed starburst age has little effect (left panel, red distribution). Therefore, assuming a value of 1 $Z_{\odot}$ would underestimate the dust content of these faint galaxies.

In the upper panel of Figure 8 we plot the estimated UV slopes versus absolute UV magnitude at 1500 Å (M_{1500}). The UV spectral slope, β, correlates with the UV magnitude, M_{1500}, such that the less luminous galaxies are bluer. The same trend has been identified in other works at higher redshifts and higher luminosities (Meurer et al. 1999; Labbé et al. 2007; Overzier et al. 2008; Wilkins et al. 2011; Bouwens et al. 2012b). Fitting the estimated β values versus UV luminosities, we find $\beta = (-0.09 \pm 0.01)M_{1500} + (-3.1 \pm 0.1)$ for our $z \sim 2$ dropout sample. We note that we removed one galaxy from our sample when fitting the reddening distribution as this galaxy had an anomalously high F625W flux. Therefore the derived reddening was quite high, even though the photometry in other bands suggested a blue spectrum.

7. DISCUSSION

We have extended the UV LF at $z \sim 2$ to the faintest magnitude limit ever obtained ($M_{1500} \sim -13$ mag), allowing

us to put a strong constraint on the UV luminosity density at the epoch of peak star formation. In the next few subsections, we will discuss the contribution of faint galaxies to the UV luminosity and star formation densities at $z \sim 2$. We will also discuss the evolution of the faint-end slope of the LF and dust extinction derived from the UV spectral slope, in comparison with other results from the literature.

7.1. Comparison with Other Space Density Measurements at $z \sim 2$

In Figure 7, we plot our binned LF with those of Reddy & Steidel (2009), Oesch et al. (2010a), Hathi et al. (2010), Sawicki (2012). We prefer to compare our LF with those of Oesch et al. (2010a) and Hathi et al. (2010), as the galaxies are selected via a Lyman break in the same F275W filter and will therefore have similar redshift distributions. The Reddy & Steidel (2009) and Sawicki (2012) samples are selected with optical data alone and are at a slightly higher average redshift ($z \sim 2.3$). Given the significant evolution in the LF at these redshifts (Oesch et al. 2010a), a direct comparison with the Reddy & Steidel (2009) and Sawicki (2012) data is not ideal but the data are plotted for reference.

If we assume that the faint-end of the LF is truly a power-law, then the fit to that power law suggest an excess of moderately bright galaxies ($M_{1500} \sim -19$ mag) in our sample compared to the measurements of Oesch et al. (2010a) and Hathi et al. (2010), though the space densities are consistent within the 1σ uncertainties. We note that both of these measurements (Oesch et al. 2010a; Hathi et al. 2010) are from the same data, a 50 arcmin^2 area in the GOODS-South region as part of the *HST* WFC3 Early Release Science (ERS) data (Windhorst et al. 2011). It is important to note that both the ERS bright galaxy sample and our sample may suffer from sample variance, because they are from single, small area fields. Though the ERS UV data covers eight times the area of our survey, they are also probing more massive galaxies, which are more highly biased and subject to sample variance. Therefore surveys in additional fields are needed to address the sample variance at both the bright and faint end of the LF.

7.2. Evolution of the Faint-end Slope

Using strong gravitational lensing, we have extended the measurement of the space density of $z \sim 2$ galaxies two orders of magnitude fainter than previous studies, allowing a more precise measure of the faint-end slope of the UV LF. In Figure 9, we compare our measurement of the faint-end slope with results at other redshifts. A general implication of this plot is that α is steeper at high redshifts than at lower redshifts. The evolution of the faint-end slope is slow between $2 < z < 7$, however it has evolved significantly between $z = 2.3$ ($\alpha \sim -1.73$; Reddy & Steidel 2009) and the present ($\alpha \sim -1.2$ Wyder et al. 2005). Our faint-end slope measurement, $\alpha = -1.74$, is nearly consistent with the estimates at higher redshifts ($2.5 < z < 4$) within the error bars. Additional sight lines and deeper selection of UV galaxies at $z \sim 1$ will help us constrain the evolution of the faint end slope over the last 10 Gyr.

7.3. Evolution of Dust in Faint Star-forming Galaxies

In the upper panel of Figure 8 we show the β versus M_{1500} relation of our sample (black line) and similarly selected samples at higher redshift (Reddy & Steidel 2009; Hathi et al. 2013; Bouwens et al. 2012b). We see the same trend
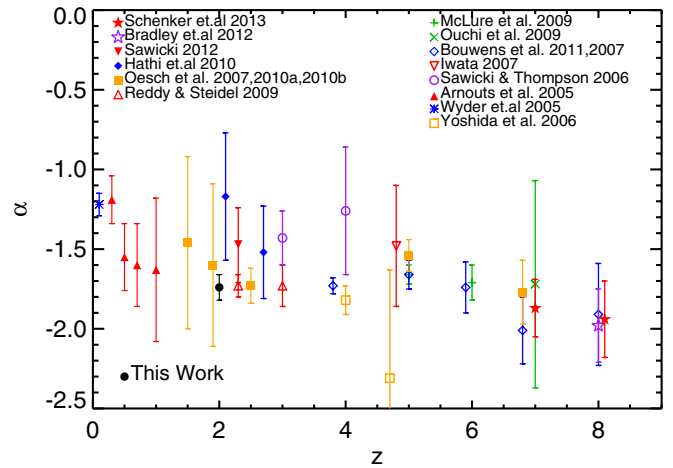
Figure 9. Evolution of the faint-end slope with redshift. The black filled circle shows our measurement of α. The plot also includes other determinations from the literature (Arnouts et al. 2005; Wyder et al. 2005; Sawicki & Thompson 2006; Yoshida et al. 2006; Bouwens et al. 2007, 2011; Iwata et al. 2007; Oesch et al. 2007, 2010a, 2010b; McLure et al. 2009; Ouchi et al. 2009; Reddy & Steidel 2009; Hathi et al. 2010; Bradley et al. 2012; Sawicki 2012; Schenker et al. 2013). The data points at $z = 8$ are all at the same redshift but have been offset slightly for clarity.

(A color version of this figure is available in the online journal.)

that is seen at higher redshifts in that fainter galaxies have bluer UV spectral slopes. The measured slope of the trend, $d\beta/dM_{1500} = -0.09 \pm 0.01$, is similar to the slopes measured at higher redshift, though the zeropoint is offset such that galaxies of the same UV luminosity are redder at later epochs. This is consistent with the trend seen from $2.5 < z < 7$ (Bouwens et al. 2012b). The increase in β at the same absolute magnitude from $z \sim 2.5$ to $z \sim 2$ (time difference of ~ 600 Myr) is about 0.4, consistent with the increase in beta from $z \sim 4$ to $z \sim 2.5$ (time difference of ~ 1 Gyr).

The luminosity-dependent UV spectral slope of Reddy & Steidel (2009) (derived from their reddening estimates) is also plotted in Figure 8 (plus symbols). Our best fit comes very close to their constant value of β at $M_{1500} \sim -19.5$ mag and consistent with the average value measured by Hathi et al. (2013) at the same redshift. The difference is that Reddy & Steidel (2009) see bluer galaxies than our sample at -19.5 mag $< M_{1500} < -18$ mag. In the faintest bin, $M_{1500} \sim -18$ mag, Reddy & Steidel (2009) state that the colors are consistent with no dust extinction, whereas we see significant extinction in galaxies at this absolute magnitude.

We believe that there are two explanations for the redder average spectral slopes exhibited in our sample compared to the Reddy & Steidel (2009) sample. First, there is a 400 Myr time difference between the average redshift of the Reddy & Steidel (2009) sample ($z = 2.3$) and our sample ($z = 2$), and we know that galaxies of the same luminosity are getting redder with time (Bouwens et al. 2012b). Second, we are likely less biased against detecting red galaxies at these absolute magnitudes. Our Lyman break selection is more complete than selections like BM/BX (Adelberger et al. 2004), which purposely target galaxies that are blue in all filters. Also, our ultra-deep imaging along with the high magnification allows us to detect redder, fainter objects at higher signal-to-noise ratio (S/N) in the bluest bands.

The measured reddening of our sample is strongly dependent on the assumed stellar population parameters, as they affect the intrinsic UV spectral slope. This is exhibited in Figure 10, where
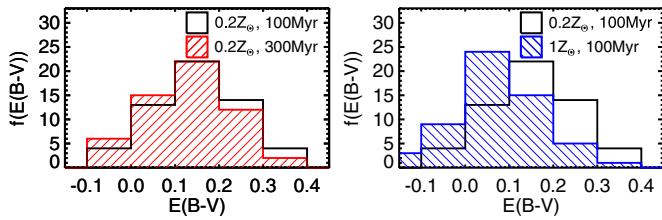
Figure 10. $E(B - V)$ distributions of the $z \sim 2$ LBG sample. The $E(B - V)$ values are derived by comparing the LBG colors with the dust reddened colors predicted by stellar population models. The black distribution is computed by assuming the realistic values for the age (100 Myr) and metallicity (0.2 $Z_\odot$) of the stellar population models (see Section 4.1). The red (left panel) and the blue (right panel) hatched histograms show the $E(B - V)$ values measured by assuming (0.2 $Z_\odot$ and 300 Myr) and (1 $Z_\odot$ and 100 Myr), respectively. The assumed age of the galaxy (left) has little effect on the derived reddening values, whereas the assumed metallicity (right) has a very large effect. If we were to assume solar metallicity, a large fraction of galaxies would have colors consistent with no extinction at all.

(A color version of this figure is available in the online journal.)

we show that changing the metallicity of the stellar population from 0.2 $Z_\odot$ to 1.0 $Z_\odot$ decreases the average color excess from $E(B - V) = 0.15$ mag to $E(B - V) = 0.08$ mag. The assumed starburst age has very little effect (average $E(B-V) = 0.15$ mag to $E(B - V) = 0.13$ mag when increasing the age from 100 to 300 Myr).

The lower value of metallicity we have used in this work, $Z = 0.2 Z_\odot$, is justified by the low stellar masses of our sample galaxies ($7 < \log(M/M_\odot) < 9$, A. Dominguez et al. 2013, in preparation) and the metallicity measurements at high and low mass at these redshifts (Erb et al. 2006; Belli et al. 2013), assuming that stellar and gas-phase metallicities are similar.

The ultimate goal in measuring the UV spectral slopes of these galaxies is to infer the extinction of the UV light in order to measure the intrinsic UV luminosities and SFRs. In the lower panel of Figure 8 we show the implied color excess, $E(B - V)$, given the intrinsic spectral slope of our fiducial model (constant star formation, age = 100 Myr, $Z = 0.2 Z_\odot$) and assuming a Calzetti attenuation curve.

Intriguingly, nearly every galaxy brighter than $M_{1500} < -15$ mag has significant reddening. The dashed line in the lower panel of Figure 8 shows the average color excess of our sample, $\langle E(B - V) \rangle = 0.15$ mag, which is similar to the value measured for much more luminous galaxies by Reddy & Steidel (2009, $E(B - V) = 0.13$ mag, plus symbols), Sawicki (2012, purple squares), and Hathi et al. (2013, $E(B - V) = 0.15$ mag, gray filled circle), who assumed solar metallicity.

Thus, we come to the important conclusion that the trend of bluer UV spectral slopes at fainter absolute magnitudes is *not* necessarily due to decreasing dust reddening. Rather, the dust reddening at faint magnitudes (-18mag $< M_{1500} < -15$ mag) is similar to the reddening in more luminous galaxies (-21mag $< M_{1500} < -18$ mag), and the bluer observed UV slopes are due to bluer *intrinsic* UV slopes because the stellar population is metal poor. Of course, the reddening likely depends on luminosity as well. In order to know the exact relation of average extinction with luminosity, we need a more accurate measure of the luminosity- (or mass) metallicity relation. Furthermore, this analysis has assumed a Calzetti attenuation curve. There is some evidence that young galaxies may have steeper attenuation curves (e.g., SMC; Siana et al. 2008b, 2009; Reddy et al. 2010). Measurements of the infrared luminosities of these faint galaxies will help determine which attenuation curve is more appropriate.

Table 4
UV Luminosity Density

Range[a]	UV Luminosity Density[b]
$[-21.68, -19.76]$[c]	$4.16^{+0.46}_{-0.49}$
$[-19.76, -12.76]$	$30.8^{+1.9}_{-3.1}$
$[-12.76, 0.00]$	$8.09^{+4.4}_{-2.4}$
$[-21.68, 0.00]$	$43.1^{+6.8}_{-6.0}$

Notes.
[a] Absolute magnitudes at 1500 Å.
[b] Units of $\times 10^{25}$ erg s^{-1} Hz^{-1} Mpc^{-3}.
[c] The Oesch et al. (2010a) limit is slightly fainter, but we only integrate to our bright limit.

In the future, measurements of metallicities (with rest-frame optical spectroscopy) and infrared luminosities will help us better understand the extinction in these faint galaxies. Because of the high magnification, these galaxies comprise an ideal sample for follow-up.

7.4. The Effect of Intracluster Dust

In this study, all of the UV-dropouts are located behind a massive cluster so the light coming from these background galaxies can be affected by intracluster dust. Recent studies of SDSS clusters (Chelouche et al. 2007; Bovy et al. 2008; Muller et al. 2008) have shown that there is a negligible amount of intracluster dust attenuation $E(B - V) < 8 \times 10^{-3}$ mag on scales smaller than 1 Mpc from the cluster center. We estimated the average intracluster dust reddening(A_λ) in the UV and optical bands to see if it has any effect on our LBG selection or spectral slope estimates. Bovy et al. (2008) measures the intracluster dust attenuation for a large sample of SDSS clusters. They calibrate the extinction curve presented in Charlot & Fall (2000), by comparing the spectra of galaxies that lie behind and adjacent to the SDSS clusters. We approximated the A_λ values based on their calibrated extinction curve. Both the UV-dropout selection and the UV spectral slope measurements are not significantly affected by intracluster reddening because the estimated color excesses are negligible ($A_{F275W} - A_{F336W} = 0.01$ mag, $A_{F475W} - A_{F625W} = 0.01$ mag).

7.5. UV Luminosity Density

In the following discussion we prefer to compare to the samples of Oesch et al. (2010a) and Hathi et al. (2010) because the samples are selected with similar filters and are at a similar redshift. If we integrate our LF over all luminosities down to zero to find the entire UV luminosity density, we get the value of $\rho_{UV} = 43.1^{+6.8}_{-6.0} \times 10^{25}$ erg s^{-1} Hz^{-1} Mpc^{-3}. A large fraction of 71% of the total luminosity density at $z = 2$ is from the luminosity range of our sample alone (-19.76 mag $< M_{1500} < -12.76$ mag). The fraction is less than 10% for galaxies in the absolute magnitude range of Oesch et al. (2010a) which are brighter than our sample ($M_{1500} < -19.76$ mag). Our most luminous galaxy is about the faintest galaxy seen in the Oesch et al. (2010a) sample, so there is very little overlap in luminosities. The faint galaxies in our sample account for seven times more UV luminosity density than the brighter galaxies from Oesch et al. (2010a). If we assume the LF has the same slope down to zero luminosity, integrating from our faintest bin down to zero only increases the UV luminosity density by 20%. All of these values are given in Table 4. We note

that extending the luminosity range to much larger luminosities adds a negligible amount to the UV luminosity density. This demonstrates the power of cluster lensing to quickly uncover the primary sources of star formation at these epochs.

7.6. Star Formation Rate Density

The evolution of the SFRD has been an ongoing subject of research, especially at $1 < z < 3$ because star formation appears to have peaked at this epoch (e.g., Calzetti & Heckman 1999; Steidel et al. 1999; Ferguson et al. 2000; Hopkins et al. 2000; Hopkins & Beacom 2006; Reddy & Steidel 2009). Because of the steep faint-end slope of the LF, much of the star formation occurs in faint galaxies. Furthermore, because of the significant extinction seen in our sample, there is even more star formation in our faint sample.

Of course, because this population is not well studied, many of the assumptions typically applied in such studies may not apply to our sample. First, as mentioned previously, the metallicity is likely significantly lower than Solar, which results in significant ($\sim 15\%$) differences in the conversion of UV luminosity density to SFRD. Second, the starburst ages may be significantly younger than 10^8 yr. For younger starbursts, the SFR is a function of both the UV luminosity and the population age. Indeed, the assumption of continuous star formation may not be accurate at all in these systems where supernovae are thought to be very effective at shutting down star formation on short time scales (e.g., Governato et al. 2012). Third, because the typical attenuation curve in such systems has not been well measured, the dust corrections are still not well understood. Given these caveats, we calculate below the best estimate of the SFRD from UV-selected galaxies at $z \sim 2$.

We use the Kennicutt (1998) conversion of the UV luminosity density to SFR as below:

$$\mathrm{SFR}\,(M_\odot\,\mathrm{yr}^{-1}) = 1.4 \times 10^{-28} L_{\mathrm{UV}}\,(\mathrm{erg\,s^{-1}Hz^{-1}}) \qquad (15)$$

where a Salpeter IMF (Salpeter 1955) from 0.1 to 100 $M_\odot$ is assumed. Using the total UV luminosity density from Table 4, we find a SFRD uncorrected for dust of 0.060 $M_\odot$ yr^{-1} Mpc^{-3}. To correct for extinction, we note that the average attenuation measured in our sample ($E(B - V) = 0.15$ mag) is similar to the values measured at the bright end by Reddy & Steidel (2009) and Hathi et al. (2013). Thus, we use this constant value to derive a factor of 4.17 correction for extinction (assuming a Calzetti attenuation curve) for galaxies of all luminosities. We therefore determine a SFRD of $0.252^{+0.040}_{-0.035}$ $M_\odot$ yr^{-1} Mpc^{-3} for UV-selected galaxies at $z \sim 2$. If we use a Kroupa (Kroupa 2001) or Chabrier (Chabrier 2003) IMF, this value needs to be divided by 1.7 or 1.8, respectively to account for the decreased number of low mass stars relative to the Salpeter IMF. We convert to a Kroupa IMF (SFRD$_{\mathrm{Kroupa}}$ = $0.148^{+0.023}_{-0.020}$ $M_\odot$ yr^{-1} Mpc^{-3}) to compare to the value estimated by Reddy & Steidel (2009, $0.122^{+0.027}_{-0.027}$ $M_\odot$ yr^{-1} Mpc^{-3}). Our value is about 20% higher but within their error bars. It is important to note however, that Reddy & Steidel (2009) use an average dust extinction correction factor of 1.91, less than half the correction that we use (4.17). Thus, if they implemented the same constant extinction correction as this paper for all UV-selected galaxies, their estimate of the SFRD would more than double. This shows the importance of the dust correction estimate for the fainter galaxies.

8. SUMMARY

The sensitive UV imaging capability of the WFC3/UVIS camera allows us to study intermediate redshift ($1 < z < 3$) star-forming galaxies. We used the deepest near-UV images ever obtained with the *HST*/UVIS channel to identify ultra-faint star-forming galaxies located behind the massive cluster A1689. We found 58 LBGs at $z \sim 2$ that are highly magnified due to strong gravitational lensing. The main conclusions of this work are summarized below:

1. The faint-end slope of the UV LF is estimated to be $\alpha = -1.74 \pm 0.08$, consistent with previous determinations at $2.3 < z < 6$ (Bouwens et al. 2007; Reddy & Steidel 2009).

2. The UV LF shows no turnover down to very faint UV magnitudes ($M_{1500} \sim -13$ mag). This is particularly interesting because the bright sources do not provide sufficient ionizing photons to ionize the universe by $z \sim 6$ (Robertson et al. 2013). Galaxies of such low luminosities are required at $z > 7$ to reionize the intergalactic hydrogen and produce the high Thompson scattering optical depth to the cosmic microwave background seen by the Wilkinson Microwave Anisotropy Probe (Kuhlen & Faucher-Giguère 2012; Robertson et al. 2013). Indeed, these faint galaxies may contribute significantly to the ionizing background at moderate redshift ($z \sim 3$, Nestor et al. 2013).

   However recent numerical simulations by Kuhlen et al. (2013) show a cutoff in the simulated UV LF at $M_{1500} = -16$, due to the suppression of the star formation in low metallicity faint galaxies. The discrepancy between our results and Kuhlen et al. (2013) is only in our two faintest magnitude bins, where the number of objects is small. Further LBG searches in more lensing clusters will provide a more robust test of this prediction.

3. The UV spectral slope, β, for these LBGs at $z \sim 2$ is redder than higher redshift determinations at the same UV luminosities. The correlation between β and the rest-frame UV magnitude implies higher dust extinction in more luminous galaxies, as is seen at higher redshifts. We find evidence for significant dust extinction, averaging $E(B - V) \sim 0.15$ mag, in most star-forming galaxies with -18mag $< M_{1500} < -15$ mag, in contrast with previous measurements at these redshifts (Reddy & Steidel 2009; Sawicki 2012). Our finding assumes a Calzetti attenuation curve and $Z = 0.2\,Z_\odot$ metallicity. Both assumptions need to be confirmed with further studies.

4. We derive a total UV luminosity density of $4.31^{+0.68}_{-0.60} \times 10^{26}$ erg s^{-1} Hz^{-1} Mpc^{-3} when integrating our LF and extrapolating to zero luminosity. More than 70% of the UV luminosity density originates from the galaxies in the luminosity range covered by our sample. We estimate that no more than 20% of the UV luminosity density originates from fainter galaxies than those in our sample.

5. Assuming a constant extinction ($E(B-V) = 0.15$ mag, UV dust correction of 4.2) for galaxies of all luminosities, we estimate the global SFRD (of UV-selected galaxies) to be $0.148^{+0.023}_{-0.020}$ $M_\odot$ yr^{-1} Mpc^{-3} (Kroupa IMF). This number is dependent on many assumptions regarding the ages, metallicities and extinction curves for this faint population of galaxies. Further investigations are required to accurately determine these properties of this new population.

REFERENCES

Adelberger, K. L., Steidel, C. C., Shapley, A. E., et al. 2004, ApJ, 607, 226
Arnouts, S., Schiminovich, D., Ilbert, O., et al. 2005, ApJL, 619, L43
Baggett, S. M., Noeske, K., Anderson, J., MacKenty, J. W., & Petro, L. 2012, Proc. SPIE, 8453, 845336
Belli, S., Jones, T., Ellis, R. S., & Richard, J. 2013, ApJ, 772, 141
Bertin, E., & Arnouts, S. 1996, A&AS, 117, 393
Bouwens, R., Bradley, L., Zitrin, A., et al. 2012a, arXiv:1211.2230
Bouwens, R. J., Illingworth, G. D., Bradley, L. D., et al. 2009, ApJ, 690, 1764
Bouwens, R. J., Illingworth, G. D., Franx, M., & Ford, H. 2007, ApJ, 670, 928
Bouwens, R. J., Illingworth, G. D., Oesch, P. A., et al. 2011, ApJ, 737, 90
Bouwens, R. J., Illingworth, G. D., Oesch, P. A., et al. 2012b, ApJ, 754, 83
Bovy, J., Hogg, D. W., & Moustakas, J. 2008, ApJ, 688, 198
Bradley, L. D., Bouwens, R. J., Ford, H. C., et al. 2008, ApJ, 678, 647
Bradley, L. D., Trenti, M., Oesch, P. A., et al. 2012, ApJ, 760, 108
Brammer, G. B., van Dokkum, P. G., & Coppi, P. 2008, ApJ, 686, 1503
Broadhurst, T. J., Taylor, A. N., & Peacock, J. A. 1995, ApJ, 438, 49
Bruzual, G., & Charlot, S. 2003, MNRAS, 344, 1000
Bunker, A. J., Stanway, E. R., Ellis, R. S., & McMahon, R. G. 2004, MNRAS, 355, 374
Bunker, A. J., Wilkins, S., Ellis, R. S., et al. 2010, MNRAS, 409, 855
Calzetti, D., Armus, L., Bohlin, R. C., et al. 2000, ApJ, 533, 682
Calzetti, D., & Heckman, T. M. 1999, ApJ, 519, 27
Calzetti, D., Kinney, A. L., & Storchi-Bergmann, T. 1994, ApJ, 429, 582
Casertano, S., de Mello, D., Dickinson, M., et al. 2000, AJ, 120, 2747
Chabrier, G. 2003, PASP, 115, 763
Charlot, S., & Fall, S. M. 2000, ApJ, 539, 718
Chelouche, D., Koester, B. P., & Bowen, D. V. 2007, ApJL, 671, L97
Coe, D., Benítez, N., Broadhurst, T., & Moustakas, L. A. 2010, ApJ, 723, 1678
Coe, D., Zitrin, A., Carrasco, M., et al. 2013, ApJ, 762, 32
Coleman, G. D., Wu, C.-C., & Weedman, D. W. 1980, ApJS, 43, 393
Conroy, C., & Wechsler, R. H. 2009, ApJ, 696, 620
Conroy, C., Wechsler, R. H., & Kravtsov, A. V. 2006, ApJ, 647, 201
Daddi, E., Cimatti, A., Renzini, A., et al. 2004, ApJ, 617, 746
Egami, E., Kneib, J.-P., Rieke, G. H., et al. 2005, ApJL, 618, L5
Erb, D. K., Shapley, A. E., Pettini, M., et al. 2006, ApJ, 644, 813
Ferguson, H. C., Dickinson, M., & Williams, R. 2000, ARA&A, 38, 667
Fynbo, J. P. U., Prochaska, J. X., Sommer-Larsen, J., Dessauges-Zavadsky, M., & Møller, P. 2008, ApJ, 683, 321
Governato, F., Zolotov, A., Pontzen, A., et al. 2012, MNRAS, 422, 1231
Haberzettl, L., Williger, G., Lehnert, M. D., Nesvadba, N., & Davies, L. 2012, ApJ, 745, 96
Hathi, N. P., Cohen, S. H., Ryan, R. E., Jr., et al. 2013, ApJ, 765, 88
Hathi, N. P., Ryan, R. E., Jr., Cohen, S. H., et al. 2010, ApJ, 720, 1708
Hopkins, A. M., & Beacom, J. F. 2006, ApJ, 651, 142
Hopkins, A. M., Connolly, A. J., & Szalay, A. S. 2000, AJ, 120, 2843
Iwata, I., Ohta, K., Tamura, N., et al. 2007, MNRAS, 376, 1557
Janknecht, E., Reimers, D., Lopez, S., & Tytler, D. 2006, A&A, 458, 427
Jones, T., Ellis, R., Jullo, E., & Richard, J. 2010, ApJL, 725, L176
Jullo, E., Kneib, J.-P., Limousin, M., et al. 2007, NJPh, 9, 447
Kennicutt, R. C., Jr. 1998, ARA&A, 36, 189
Kim, T.-S., Hu, E. M., Cowie, L. L., & Songaila, A. 1997, AJ, 114, 1
Kneib, J.-P., Ellis, R. S., Santos, M. R., & Richard, J. 2004, ApJ, 607, 697
Koekemoer, A. M., Fruchter, A. S., Hook, R. N., & Hack, W. 2003, in HST Calibration Workshop: Hubble after the Installation of the ACS and the NICMOS Cooling System, ed. S. Arribas, A. Koekemoer, & B. Whitmore (Baltimore, MD: STScI), 337

Kroupa, P. 2001, MNRAS, 322, 231
Kuhlen, M., & Faucher-Giguère, C.-A. 2012, MNRAS, 423, 862
Kuhlen, M., Madau, P., & Krumholz, M. 2013, ApJ, 776, 34
Labbé, I., Franx, M., Rudnick, G., et al. 2007, ApJ, 665, 944
Law, D. R., Steidel, C. C., Shapley, A. E., et al. 2012, ApJ, 759, 29
Leitherer, C., Schaerer, D., Goldader, J. D., et al. 1999, ApJS, 123, 3
Lilly, S. J., Le Fevre, O., Hammer, F., & Crampton, D. 1996, ApJL, 460, L1
Limousin, M., Richard, J., Jullo, E., et al. 2007, ApJ, 668, 643
Ly, C., Malkan, M. A., Treu, T., et al. 2009, ApJ, 697, 1410
Madau, P. 1995, ApJ, 441, 18
Madau, P., Ferguson, H. C., Dickinson, M. E., et al. 1996, MNRAS, 283, 1388
Magnelli, B., Elbaz, D., Chary, R. R., et al. 2011, A&A, 528, A35
McLure, R. J., Cirasuolo, M., Dunlop, J. S., Foucaud, S., & Almaini, O. 2009, MNRAS, 395, 2196
Meurer, G. R., Heckman, T. M., & Calzetti, D. 1999, ApJ, 521, 64
Moller, P., & Jakobsen, P. 1990, A&A, 228, 299
Muller, S., Wu, S.-Y., Hsieh, B.-C., et al. 2008, ApJ, 680, 975
Narayan, R., Blandford, R., & Nityananda, R. 1984, Natur, 310, 112
Nestor, D. B., Shapley, A. E., Kornei, K. A., Steidel, C. C., & Siana, B. 2013, ApJ, 765, 47
Nestor, D. B., Shapley, A. E., Steidel, C. C., & Siana, B. 2011, ApJ, 736, 18
Noeske, K., Baggett, S., Bushouse, H., et al. 2012, WFC3 UVIS Charge Transfer Eciency October 2009 to October 2011, Tech. rep
Oesch, P. A., Bouwens, R. J., Carollo, C. M., et al. 2010a, ApJL, 725, L150
Oesch, P. A., Bouwens, R. J., Illingworth, G. D., et al. 2010b, ApJL, 709, L16
Oesch, P. A., Stiavelli, M., Carollo, C. M., et al. 2007, ApJ, 671, 1212
Oke, J. B., & Gunn, J. E. 1983, ApJ, 266, 713
O'Meara, J. M., Prochaska, J. X., Worseck, G., Chen, H.-W., & Madau, P. 2013, ApJ, 765, 137
Ouchi, M., Mobasher, B., Shimasaku, K., et al. 2009, ApJ, 706, 1136
Overzier, R. A., Bouwens, R. J., Cross, N. J. G., et al. 2008, ApJ, 673, 143
Pettini, M., Rix, S. A., Steidel, C. C., et al. 2002, Ap&SS, 281, 461
Pickles, A. J. 1998, yCat, 611, 863
Rao, S. M., Turnshek, D. A., & Nestor, D. B. 2006, ApJ, 636, 610
Reddy, N. A., Erb, D. K., Pettini, M., Steidel, C. C., & Shapley, A. E. 2010, ApJ, 712, 1070
Reddy, N. A., & Steidel, C. C. 2009, ApJ, 692, 778
Reddy, N. A., Steidel, C. C., Fadda, D., et al. 2006, ApJ, 644, 792
Reddy, N. A., Steidel, C. C., Pettini, M., et al. 2008, ApJS, 175, 48
Ribaudo, J., Lehner, N., & Howk, J. C. 2011, ApJ, 736, 42
Richard, J., Kneib, J.-P., Ebeling, H., et al. 2011, MNRAS, 414, L31
Richard, J., Stark, D. P., Ellis, R. S., et al. 2008, ApJ, 685, 705
Rix, H.-W., Barden, M., Beckwith, S. V. W., et al. 2004, ApJS, 152, 163
Robertson, B. E. 2010, ApJ, 713, 1266
Robertson, B. E., Furlanetto, S. R., Schneider, E., et al. 2013, ApJ, 768, 71
Salpeter, E. E. 1955, ApJ, 121, 161
Sandage, A., Tammann, G. A., & Yahil, A. 1979, ApJ, 232, 352
Sawicki, M. 2012, MNRAS, 421, 2187
Sawicki, M., & Thompson, D. 2006, ApJ, 642, 653
Schenker, M. A., Robertson, B. E., Ellis, R. S., et al. 2013, ApJ, 768, 196
Shapley, A. E., Steidel, C. C., Erb, D. K., et al. 2005, ApJ, 626, 698
Siana, B., Polletta, M. d. C., Smith, H. E., et al. 2008a, ApJ, 675, 49
Siana, B., Smail, I., Swinbank, A. M., et al. 2009, ApJ, 698, 1273
Siana, B., Teplitz, H. I., Chary, R.-R., Colbert, J., & Frayer, D. T. 2008b, ApJ, 689, 59
Stark, D. P., Ellis, R. S., Richard, J., et al. 2007, ApJ, 663, 10
Stark, D. P., Swinbank, A. M., Ellis, R. S., et al. 2008, Natur, 455, 775
Steidel, C. C., Adelberger, K. L., Giavalisco, M., Dickinson, M., & Pettini, M. 1999, ApJ, 519, 1
Teplitz, H. I., Rafelski, M., Kurczynski, P., et al. 2013, AJ, 146, 159
Tody, D. 1986, Proc. SPIE, 627, 733
Wilkins, S. M., Bunker, A. J., Stanway, E., Lorenzoni, S., & Caruana, J. 2011, MNRAS, 417, 717
Windhorst, R. A., Cohen, S. H., Hathi, N. P., et al. 2011, ApJS, 193, 27
Wyder, T. K., Treyer, M. A., Milliard, B., et al. 2005, ApJL, 619, L15
Yan, H., Dickinson, M., Giavalisco, M., et al. 2006, ApJ, 651, 24
Yan, H.-J., Windhorst, R. A., Hathi, N. P., et al. 2010, RAA, 10, 867
Yoshida, M., Shimasaku, K., Kashikawa, N., et al. 2006, ApJ, 653, 988
Yuan, T.-T., Kewley, L. J., & Richard, J. 2013, ApJ, 763, 9
Zheng, W., Postman, M., Zitrin, A., et al. 2012, Natur, 489, 406
Zitrin, A., Moustakas, J., Bradley, L., et al. 2012, ApJL, 747, L9